ORIGINAL ARTICLE

Triple-frequency carrier phase precise time and frequency transfer models for BDS-3

Ke Su[1,2] · Shuanggen Jin[1,3]

Abstract

The third-generation BeiDou navigation satellite system (BDS-3) began providing global positioning, navigation and timing service on December 27, 2018. We present three triple-frequency carrier phase (CP) precise time and frequency transfer models using the BDS-3 B1I/B3I/B2a signals, named IF-PPP1, IF-PPP2 and UC-PPP models, respectively. The BDS B1I/B3I dual-frequency ionospheric-free (IF) model is also introduced, known as IF-PPP0 model. The corresponding mathematical and stochastic models are developed. Two stations located at time laboratories and connected to a high-precision atomic clock are utilized to assess the performances of the proposed CP precise time and frequency transfer models. In addition, the number of visible satellites, position dilution of precision, time dilution of precision, estimated positioning errors, zenith tropospheric delay and inter-frequency bias for two stations are also analyzed. The results show that BDS CP precise time and frequency transfer can achieve better performances with increasing number of BDS-3 observations. The proposed models all can be applied for precise time and frequency transfer with the BDS-3 triple-frequency signals, with stability and accuracy identical to the BDS IF-PPP0 solution. The stability of 10,000 s for the proposed BDS CP precise time and frequency models is better than 1.5×10^{-14}.

Keywords BDS-3 · Carrier phase · Precise time and frequency transfer · Precise point positioning · Allan deviation

Introduction

The earlier GPS and GLONASS satellites were designed to provide signals on two frequencies. With the rapid development and modernization of the Global Navigation Satellite System (GNSS), the users have the choice to use three or more frequency signals. For instance, the new generation GPS satellites, namely Block IIF satellites, are transmitting the third signal L5 (1176.45 MHz) in addition to the existing L1 (1575.42 MHz) and L2 (1227.60 MHz) signals

✉ Ke Su
   ksu@shao.ac.cn

   Shuanggen Jin
   sgjin@shao.ac.cn; sg.jin@yahoo.com

[1] Shanghai Astronomical Observatory, Chinese Academy of Sciences, Shanghai 200030, China

[2] University of Chinese Academy of Sciences, Beijing 100049, China

[3] School of Remote Sensing and Geomatics Engineering, Nanjing University of Information Science and Technology, Nanjing 210044, China

(Montenbruck et al. 2011). Similarly, all GLONASS-K satellites and part of GLONASS-M satellites series have started to transmit signal on G3 (1202.025 MHz) after 2011 (Zaminpardaz et al. 2017). In addition, the Europe Galileo system was designed to provide signals in five frequencies centered at E1 (1575.42 MHz), E5a (1176.45 MHz), E5b (1207.14 MHz), E5 (1191.795 MHz) and E6 (1278.75 MHz) for civilian and commercial service (Wang et al. 2018).

The Chinese BeiDou Navigation Satellite System (BDS) follows a three-step strategy, including the demonstration system (BDS-1), the regional system (BDS-2), and the global system (BDS-3) (Yang et al. 2011). Since the end of 2012, the BDS-2 has comprised a constellation of five satellites in a geostationary orbit (GEO), five satellites in an inclined geostationary orbit (IGSO), and four satellites in a medium earth orbit (MEO), which can transmit signals on three bands, namely B1I at 1561.098 MHz, B2I at 1207.14 MHz, and B3I at 1268.52 MHz, respectively (Montenbruck et al. 2013). The recent BDS-3 has provided global services since December 27, 2018, and is expected to consist of 5 GEO, 3 IGSO and 27 MEO in 2020, capable of broadcasting several new signals, including B1C at 1575.42 MHz,

B2a at 1176.45 MHz, and B2b at 1207.14 MHz, respectively (Xiao et al. 2016). The B2I transmitted by the BDS-2 satellites will be replaced by the B2a signal on the BDS-3 satellites (CSNO 2019).

Thus far, the BDS satellites can operate with three or even more frequencies, which have a wide potential to benefit the ambiguity resolution, cycle detection, precise positioning, and timing. For GNSS time and frequency transfer, most timing laboratories utilize the common view (CV) and all in view (AV) techniques (Jiang and Petit 2004; Petit and Jiang 2007). The CV technique collects the signals from the same satellites to remove the common satellite errors. Hence, the distances of the stations are limited, and the accuracy of CV time transfer is only 1–10 ns (Larson and Levine 1999). Unlike CV, the AV technique is not affected by the distance between the stations and allows precise time and frequency transfer at any locations (Yao et al. 2015). For high-precision time and frequency transfer, carrier phase (CP) precise point positioning (PPP) is a typical AV technique to determine the time transfer solution, which has an accuracy ranging from the sub-nanosecond to nanosecond level (Defraigne et al. 2015).

Thanks to precise products provided by institutions such as the international GNSS service (IGS), multi-GNSS PPP time and frequency transfer is of great interest in the time community. For example, Ge et al. (2018) investigated GLONASS-only PPP transfer considering the strategies of inter-frequency code biases, showing that the standard deviation (STD) of the difference between GLONASS-only and GPS-only PPP was approximately 0.4 ns. Defraigne and Baire (2011) present a combined GPS and GLONASS time transfer, indicating that adding the observations of GLONASS can modify the time and frequency transfer results and improve short-term stability. Zhang et al. (2019) performed Galileo-only time transfer with prior constraint information. The results indicated that the STD improved by 47.6% and 51.4%, respectively, using station coordinates and troposphere zenith delay constraint. Also, Tu et al. (2018) demonstrated that the triple-frequency BDS-2 PPP model can be applied for CP precise time and frequency transfer with accuracy and stability identical to the dual-frequency ionospheric-free (IF) PPP model. However, the performances of CP precise time and frequency transfer with BDS-3 observations were not investigated. With the upgrade and further development of the BDS, new challenges arise for processing the multi-frequency BDS-3 signals in CP precise time and frequency models. In general, the new signals are expected to be beneficial to enhancing the accuracy and stability of time and frequency transfer.

With this background, we present three triple-frequency CP precise time and frequency models for BDS B1I, B3I and B2a signals. The BDS-2 and BDS B1I/B3I dual-frequency IF PPP solutions are also conducted for the convenience of comparison. First, we developed the mathematical and stochastic

models of BDS CP precise time and frequency. Then, the performances of BDS CP precise time and frequency are validated and compared with the experimental datasets from a time link. In particular, the number of visible satellites, position dilution of precision (PDOP), time dilution of precision (TDOP), estimated positioning errors, zenith tropospheric delay (ZTD), and inter-frequency bias (IFB) are also analyzed. Finally, some conclusions and discussions are given.

Methodology

We begin with the general observation models for BDS (BDS-2/BDS-3) signals. Then, four BDS CP precise time and frequency models are developed in detail. The section ends with the characteristic of different models.

General observation models

CP precise time and frequency transfer usually uses the PPP model. The linearized equations of observations between the receiver and satellite on a single frequency for BDS can be expressed as (Leick et al. 2015):

$$p_{r,j}^s = u_r^s \cdot x + dt_r - dt^s + M_w \cdot Z_w + I_{r,j}^s + d_{r,j} + d_j^s + \varepsilon_p \quad (1)$$

$$l_{r,j}^s = u_r^s \cdot x + dt_r - dt^s + M_w \cdot Z_w - I_{r,j}^s + \lambda_j \cdot N_{r,j}^s + b_{r,j} - b_j^s + \varepsilon_\varphi \quad (2)$$

where indices s, r, and j ($j = 1, 2, 3$) refer to the BDS satellite, receiver, and corresponding frequency band (B1I, B3I, and B2a), respectively; $p_{r,j}^s$ and $l_{r,j}^s$ denote the observed-minus-computed values of the pseudorange and CP observations, respectively; u_r^s denotes the unit vector of the component from the receiver to the satellite; x denotes the vector of the receiver position increments in three dimensions; dt_r and dt^s denote the receiver and satellite clock offset, respectively; M_w denotes the wet mapping functions; Z_w denotes the zenith wet delay (ZWD); λ_j is the wavelength of CP on jth frequency; $I_{r,j}^s$ is the slant ionospheric delay on the jth frequency f_j^s. It is possible to convert the first-order ionospheric delays to different frequencies by the frequency-dependent multiplier factor $\gamma_k^s = (f_1^s/f_k^s)^2$, $k = 2, 3$; $N_{r,j}^s$ is the integer ambiguity on the jth frequency; $d_{r,j}$ and d_j^s are the uncalibrated code delays (UCDs) with respect to receiver and satellite, respectively; $b_{r,j}$ and b_j^s are the uncalibrated phase delays (UPDs) with respect to receiver and satellite, respectively. ε_p and ε_φ are the pseudorange and CP observation noises including multipath, respectively.

Using the notations:

$$\alpha_{m,n}^s = (f_m^s)^2/[(f_m^s)^2 - (f_n^s)^2], \quad \beta_{m,n}^s = -(f_n^s)^2/[(f_m^s)^2 - (f_n^s)^2] \quad (3)$$

$$\text{DCB}^s_{m,n} = d^s_m - d^s_n, \quad \text{DCB}_{r,m,n} = d_{r,m} - d_{r,n} \tag{4}$$

the IF functions can be written as

$$p^s_{r,\text{IF}_{m,n}} = \alpha^s_{m,n} \cdot p^s_{r,m} + \beta^s_{m,n} \cdot p^s_{r,n}, \quad l^s_{r,\text{IF}_{m,n}} = \alpha^s_{m,n} \cdot l^s_{r,m} + \beta^s_{m,n} \cdot l^s_{r,n} \tag{5}$$

$$\begin{aligned} p^s_{r,\text{IF}_{1,2,3}} &= e_1 \cdot p^s_{r,1} + e_2 \cdot p^s_{r,2} \\ &+ e_3 \cdot p^s_{r,3}, \quad l^s_{r,\text{IF}_{1,2,3}} = e_1 \cdot l^s_{r,1} \\ &+ e_2 \cdot l^s_{r,2} + e_3 \cdot l^s_{r,3} \end{aligned} \tag{6}$$

with

$$d^s_{\text{IF}_{m,n}} = \alpha^s_{m,n} \cdot d^s_m + \beta^s_{m,n} \cdot d^s_n, \quad d_{r,\text{IF}_{m,n}} = \alpha^s_{m,n} \cdot d_{r,m} + \beta^s_{m,n} \cdot d_{r,n} \tag{7}$$

$$\begin{aligned} d^s_{\text{IF}_{1,2,3}} &= e_1 \cdot d^s_1 + e_2 \cdot d^s_2 + e_3 \cdot d^s_3, \\ d_{r,\text{IF}_{1,2,3}} &= e_1 \cdot d_{r,1} \\ &+ e_2 \cdot d_{r,2} + e_3 \cdot d_{r,3} \end{aligned} \tag{8}$$

$$b^s_{\text{IF}_{m,n}} = \alpha^s_{m,n} \cdot b^s_m + \beta^s_{m,n} \cdot b^s_n, \quad b_{r,\text{IF}_{m,n}} = \alpha^s_{m,n} \cdot b_{r,m} + \beta^s_{m,n} \cdot b_{r,n} \tag{9}$$

$$\begin{aligned} b^s_{\text{IF}_{1,2,3}} &= e_1 \cdot b^s_1 + e_2 \cdot b^s_2 + e_3 \cdot b^s_3, \\ b_{r,\text{IF}_{1,2,3}} &= e_1 \cdot b_{r,1} + e_2 \cdot b_{r,2} + e_3 \cdot b_{r,3} \end{aligned} \tag{10}$$

where $\alpha^s_{m,n}$, $\beta^s_{m,n}$ are frequency factors ($m, n = 1, 2, 3$; $m \neq n$); e_1, e_2 and e_3 are the combination coefficients for the triple-frequency PPP model based on a single IF combination; $\text{DCB}^s_{m,n}$ and $\text{DCB}_{r,m,n}$ are the satellite and receiver differential code bias (DCB) between pseudoranges on the frequency bands m and n.

IF-PPP0: IF model with a single dual-frequency combination

The dual-frequency IF combination can be generated by BDS B1I and B3I signals. The model, namely IF-PPP0, for the dual-frequency IF observations can be written as:

$$\begin{cases} p^s_{r,\text{IF}_{1,2}} = u^s_r \cdot x + d\bar{t}_r + M_w \cdot Z_w \\ l^s_{r,\text{IF}_{1,2}} = u^s_r \cdot x + d\bar{t}_r + M_w \cdot Z_w + \lambda_1 \cdot \bar{N}^s_{r,\text{IF}_{1,2}} \end{cases} \tag{11}$$

with

$$\begin{cases} d\bar{t}_r = dt_r + d_{r,\text{IF}_{1,2}} \\ \lambda_1 \cdot \bar{N}^s_{r,\text{IF}_{1,2}} = \alpha^s_{1,2} \cdot \lambda_1 \cdot N^s_{r,1} + \beta^s_{1,2} \cdot \lambda_2 \cdot N^s_{r,2} + b_{r,\text{IF}_{1,2}} - b^s_{\text{IF}_{1,2}} - d_{r,\text{IF}_{1,2}} \end{cases} \tag{12}$$

The estimated parameters in IF-PPP0 model include receiver positions, receiver clocks, ZWD, and float ambiguities, which can be expressed as:

$$E_{\text{IF-PPP0}} = \begin{bmatrix} x & d\bar{t}_r & Z_w & \bar{N}^s_{r,\text{IF}_{1,2}} \end{bmatrix} \tag{13}$$

where $E_{\text{IF-PPP0}}$ denotes the estimable vector of the IF-PPP0 model.

IF-PPP1: IF model with two dual-frequency IF combinations

The observations for the BDS B1I, B3I and B2a signals can be combined by any of the two dual-frequency IF combinations. Considering that two of the three combinations are independent and noise amplification of the B3I/B2a is the largest, we utilized the combinations of B1I/B3I and B1I/B2a and call this model IF-PPP1. Then, the linearized observation equations of the IF-PPP1 model can be written as:

$$\begin{cases} p^s_{r,\text{IF}_{1,2}} = u^s_r \cdot x + d\bar{t}_r + M_w \cdot Z_w \\ l^s_{r,\text{IF}_{1,2}} = u^s_r \cdot x + d\bar{t}_E + M_w \cdot Z_w + \lambda_1 \cdot \bar{N}^s_{r,\text{IF}_{1,2}} \\ p^s_{r,\text{IF}_{1,3}} = u^s_r \cdot x + d\bar{t}_r + M_w \cdot Z_w + \text{ifb}_{\text{IF1}} \\ l^s_{r,\text{IF}_{1,3}} = u^s_r \cdot x + d\bar{t}_r + M_w \cdot Z_w + \lambda_1 \cdot \bar{N}^s_{r,\text{IF}_{1,3}} \end{cases} \tag{14}$$

with

$$\begin{cases} d\bar{t}_r = dt_r + d_{r,\text{IF}_{1,2}} \\ \text{ifb}_{\text{IF1}} = \beta^s_{1,2} \cdot \text{DCB}_{r,\text{IF}_{1,2}} - \beta^s_{1,3} \cdot \text{DCB}_{r,\text{IF}_{1,3}} \\ \lambda_1 \cdot \bar{N}^s_{r,\text{IF}_{1,k}} = \alpha^s_{1,k} \cdot \lambda_1 \cdot N^s_{r,1} + \beta^s_{1,k} \cdot \lambda_k \cdot N^s_{r,k} + b_{r,\text{IF}_{1,k}} - b^s_{\text{IF}_{1,k}} - d_{r,\text{IF}_{1,2}} \end{cases} \tag{15}$$

The equations of the IF-PPP1 model share the same estimable receiver clock as the dual-frequency IF PPP at the signals of B1I and B3I. An estimable IFB parameter is mandatory for the IF-PPP1 model to mitigate the inconsistency of the receiver UCDs between B1I/B3I and B1I/B2a. Hence, the estimated parameters in the IF-PPP1 model include the receiver positions, receiver clocks, ZWD, IFB, and float ambiguities, which can be expressed as:

$$E_{\text{IF-PPP1}} = \begin{bmatrix} x & d\bar{t}_r & Z_w & \text{ifb}_{\text{IF1}} & \bar{N}^s_{r,\text{IF}_{1,2}} & \bar{N}^s_{r,\text{IF}_{1,3}} \end{bmatrix} \tag{16}$$

where $E_{\text{IF-PPP1}}$ denotes the estimable vector for IF-PPP1 model.

IF-PPP2: IF model with a single triple-frequency combination

The observations for the BDS B1I, B3I and B2a signals can be integrated into a single arbitrary combination. The model, namely IF-PPP2 in this study, uniquely determines the combination coefficients e_1, e_2, and e_3 with the criteria that the

solution is geometry-free (GF), IF, and has minimum noise, based on the conditions:

$$\begin{cases} e_1 + e_2 + e_3 = 1 \\ e_1 + \gamma_2^s \cdot e_2 + \gamma_3^s \cdot e_3 = 0 \\ (e_1^2 + e_2^2 + e_3^2) = \varepsilon^2 = \min \end{cases} \tag{17}$$

Satisfying the above three condition, the coefficients e_1, e_2 and e_3 can be determined as:

$$\begin{cases} e_1 = \frac{(\gamma_2^s)^2 + (\gamma_3^s)^2 - \gamma_2^s - \gamma_3^s}{2 \cdot [(\gamma_2^s)^2 + (\gamma_3^s)^2 - \gamma_2^s \cdot \gamma_3^s - \gamma_2^s - \gamma_3^s + 1]} \\ \\ e_2 = \frac{(\gamma_3^s)^2 - \gamma_2^s \cdot \gamma_3^s - \gamma_2^s + 1}{2 \cdot [(\gamma_2^s)^2 + (\gamma_3^s)^2 - \gamma_2^s \cdot \gamma_3^s - \gamma_2^s - \gamma_3^s + 1]} \\ \\ e_3 = \frac{(\gamma_2^s)^2 - \gamma_2^s \cdot \gamma_3^s - \gamma_3^s + 1}{2 \cdot [(\gamma_2^s)^2 + (\gamma_3^s)^2 - \gamma_2^s \cdot \gamma_3^s - \gamma_2^s - \gamma_3^s + 1]} \end{cases} \tag{18}$$

Currently, only BDS-3 satellites have the capability of B2a transmission. It is impossible to conduct the PPP processing with B1I/B3I/B2a combined alone when utilizing BDS-2 observations. Therefore, the B1I/B3I IF observations are also introduced for BDS-2 so that the combined BDS PPP solutions can be achieved. The linearized observation equations of the BDS-3 and the BDS-2 satellites, respectively, for IF-PPP2 model can be written as:

$$\begin{cases} p_{r,\mathrm{IF}_{1,2,3}}^s = u_r^s \cdot x + d\bar{t}_r + M_w \cdot Z_w \\ l_{r,\mathrm{IF}_{1,2,3}}^s = u_r^s \cdot x + d\bar{t}_r + M_w \cdot Z_w + \lambda_1 \cdot \bar{N}_{r,\mathrm{IF}_{1,2,3}}^s \end{cases} \tag{19}$$

$$\begin{cases} p_{r,\mathrm{IF}_{1,2}}^s = u_r^s \cdot x + d\bar{t}_r + M_w \cdot Z_w + \mathrm{ifb}_{\mathrm{IF2}_{1,2}} \\ l_{r,\mathrm{IF}_{1,2}}^s = u_r^s \cdot x + d\bar{t}_r + M_w \cdot Z_w + \lambda_1 \cdot \bar{N}_{r,\mathrm{IF}_{1,2}}^s \end{cases} \tag{20}$$

with

$$\begin{cases} d\bar{t}_r = dt_r + d_{r,\mathrm{IF}_{1,2,3}} \\ \lambda_1 \cdot \bar{N}_{r,\mathrm{IF}_{1,2,3}}^s = e_1 \cdot \lambda_1 \cdot N_{r,1}^s + e_2 \cdot \lambda_2 \cdot N_{r,2}^s + e_3 \cdot \lambda_3 \cdot N_{r,3}^s + b_{r,\mathrm{IF}_{1,2,3}} - b_{\mathrm{IF}_{1,2,3}}^s - d_{r,\mathrm{IF}_{1,2,3}} \\ \mathrm{ifb}_{\mathrm{IF2}_{1,2}} = d_{r,\mathrm{IF}_{1,2}} - d_{r,\mathrm{IF}_{1,2,3}} \\ \lambda_1 \cdot \bar{N}_{r,\mathrm{IF}_{1,2}}^s = \alpha_{1,2}^s \cdot \lambda_1 \cdot N_{r,1}^s + \beta_{1,2}^s \cdot \lambda_k \cdot N_{r,k}^s + b_{r,\mathrm{IF}_{1,2}} - b_{\mathrm{IF}_{1,2}}^s - d_{r,\mathrm{IF}_{1,2,3}} \end{cases} \tag{21}$$

To mitigate the inconsistency of the receiver UCDs between the B1I/B3I/B2a and B1I/B3I combinations, an estimable IFB parameter is also introduced into the IF-PPP2 model. It deserves to be mentioned that the IFB parameter does not need to be considered when PPP is achieved with only BDS-3 observations. The parameters to be estimated in IF-PPP2 model include the receiver positions, receiver clocks, ZWD, IFB, and float ambiguities, which can be expressed as:

$$E_{\mathrm{IF\text{-}PPP2}} = \begin{bmatrix} x & d\bar{t}_r & Z_w & \mathrm{ifb}_{\mathrm{IF2}_{1,2}} & \bar{N}_{r,\mathrm{IF}_{1,2}}^s & \bar{N}_{r,\mathrm{IF}_{1,3}}^s \end{bmatrix} \tag{22}$$

where $E_{\mathrm{IF\text{-}PPP2}}$ denotes the estimable vector for IF-PPP2 model.

UC-PPP: model using triple-frequency uncombined observations

The linearized observation equations of uncombined (UC) triple-frequency PPP, namely UC-PPP, can be written as:

$$\begin{cases} p_{r,1}^s = u_r^s \cdot x + d\bar{t}_r + M_w \cdot Z_w + \bar{I}_{r,1}^s \\ l_{r,1}^s = u_r^s \cdot x + d\bar{t}_r + M_w \cdot Z_w - \bar{I}_{r,1}^s + \lambda_1 \cdot \bar{N}_{r,1}^s \\ p_{r,2}^s = u_r^s \cdot x + d\bar{t}_r + M_w \cdot Z_w + \gamma_2^s \cdot \bar{I}_{r,1}^s \\ l_{r,2}^s = u_r^s \cdot x + d\bar{t}_r + M_w \cdot Z_w - \gamma_2^s \cdot \bar{I}_{r,1}^s + \lambda_2 \cdot \bar{N}_{r,2}^s \\ p_{r,3}^s = u_r^s \cdot x + d\bar{t}_r + M_w \cdot Z_w + \mathrm{ifb}_{\mathrm{UC}} + \gamma_3^s \cdot \bar{I}_{r,1}^s \\ l_{r,3}^s = u_r^s \cdot x + d\bar{t}_r + M_w \cdot Z_w - \gamma_3^s \cdot \bar{I}_{r,1}^s + \lambda_3 \cdot \bar{N}_{r,3}^s \end{cases} \tag{23}$$

with

$$\begin{cases} d\bar{t}_r = dt_r + d_{r,\mathrm{IF}_{1,2}} \\ \bar{I}_{r,1}^s = I_{r,1}^s + \beta_{1,2}^s \cdot \mathrm{DCB}_{r,1,2} \\ \mathrm{ifb}_{\mathrm{UC}} = \beta_{1,2}^s / \beta_{1,3}^s \cdot \mathrm{DCB}_{r,1,2} - \mathrm{DCB}_{r,1,3} \\ \lambda_1 \cdot \bar{N}_{r,1}^s = \lambda_1 \cdot N_{r,1}^s + b_{r,1} - b_1^s + (\beta_{1,2}^s - \alpha_{1,2}^s) \cdot d_{r,1} - 2 \cdot \beta_{1,2}^s \cdot d_{r,2} \\ \lambda_2 \cdot \bar{N}_{r,2}^s = \lambda_2 \cdot N_{r,2}^s + b_{r,2} - b_2^s - 2 \cdot \alpha_{1,2}^s \cdot d_{r,1} + (\alpha_{1,2}^s - \beta_{1,2}^s) \cdot d_{r,2} \\ \lambda_3 \cdot \bar{N}_{r,3}^s = \lambda_3 \cdot N_{r,3}^s + b_{r,3} - b_3^s + (\gamma_3^s \cdot \beta_{1,2}^s - \alpha_{1,2}^s) \cdot d_{r,1} - (\beta_{1,2}^s + \gamma_3^s \cdot \beta_{1,2}^s) \cdot d_{r,2} \end{cases} \tag{24}$$

Unlike the other models, the slant ionospheric delays are estimated as unknown parameters. The ionospheric delay and receiver DCB are linearly related and estimated as lumped terms. For the triple-frequency UC model, the effects of the DCB on the third pseudoranges cannot be fully absorbed. Additional IFB parameters are introduced into the UC-PPP model to compensate the effects. Comparing (15), (21), and (24), we can see that the IFB estimates in IF-PPP1, IF-PPP2, and UC-PPP are different. The parameters to be estimated in the UC-PPP model include the receiver positions, receiver clocks, ZWD, IFB, slant ionospheric delays and float ambiguities, which can be expressed as:

$$E_{\text{UC-PPP}} = \begin{bmatrix} x & d\bar{t}_r & Z_w & \text{ifb}_{\text{UC}} & \bar{I}^s_{r,1} & \bar{N}^s_{r,1} & \bar{N}^s_{r,2} & \bar{N}^s_{r,3} \end{bmatrix} \tag{25}$$

where $E_{\text{UC-PPP}}$ denotes the estimable vector for UC-PPP model.

Characteristic of precise time and frequency transfer models

As to the precision of the BDS satellite measurements, the elevation-dependent weighting scheme can be applied for precise time and frequency transfer models. Under the assumptions that the observations are uncorrelated and share a same prior noise, the variance–covariance matrix of the observations in UC-PPP model can be expressed as:

$$\sum_{\text{UC-PPP}} = \delta_0^2 \cdot I \tag{26}$$

where $\delta_0 = a/\sin(E)$, in which a is a constant and generally set to be 0.002–0.004 m for CP and 0.2–4.0 m for code observations; E is the satellite elevation angle; I is the identity matrix. The stochastic models of the observations for other PPP models can be obtained through the error propagation law. The variance–covariance of the satellite observations for IF-PPP0, IF-PPP1 and IF-PPP2 models can be expressed as:

$$\begin{cases} \sum_{\text{IF-PPP0}_{1,2}} = \delta_0^2 \cdot [(\alpha^s_{1,2})^2 + (\beta^s_{1,2})^2] \\ \sum_{\text{IF-PPP1}_{1,2,3}} = \delta_0^2 \cdot \begin{bmatrix} (\alpha^s_{1,2})^2 + (\beta^s_{1,2})^2 & \alpha^s_{1,2} \cdot a^s_{1,3} \\ \alpha^s_{1,2} \cdot a^s_{1,3} & (\alpha^s_{1,3})^2 + (\beta^s_{1,3})^2 \end{bmatrix} \\ \sum_{\text{IF-PPP2}_{1,2,3}} = \delta_0^2 \cdot [(e_1)^2 + (e_2)^2 + (e_3)^2] \end{cases} \tag{27}$$

Table 1 summarizes the major characteristics of multi-frequency CP precise time and frequency models, including the signal combination, combination coefficients and noise amplification factor. As shown in the table, the B1I/B2a combination provides smaller a priori noise amplification than the B1I/B3I in IF-PPP1 model. The correlation index of B1I/B2a and B1I/B3I in BDS is 0.726. The IF-PPP1 and

Table 1 Characteristics of dual- and triple-frequency BDS PPP models

Models	Signal combination	e_1	e_2	e_3	Noise amplification
IF-PPP0	B1I–B3I	2.944	− 1.944	0.000	3.527
IF-PPP1	B1I–B3I	2.944	− 1.944	0.000	3.527
	B1I–B2a	2.314	0.000	− 1.314	2.662
IF-PPP2	B1I–B3I–B2a	2.343	− 0.089	− 1.254	2.659
UC-PPP	B1I	1.000	0.000	0.000	1.000
	B3I	0.000	1.000	0.000	1.000
	B2a	0.000	0.000	1.000	1.000

UC-PPP models are more flexible than the IF-PPP2 model when a particular frequency is absent. The comparison coefficients in the table show that the IF-PPP2 model is more like a B1I/B2a dual-frequency PPP model for the lower contribution of the second-frequency observations. Nevertheless, the observation noise amplification of the IF-PPP2 model is smaller than that of the IF-PPP0 and IF-PPP1 models.

Data processing strategies

To validate the performances of BDS-3 CP precise time and frequency transfer with the proposed models, observations of stations NTSC and BRCH provided by the international GNSS continuous Monitoring and Assessment System (iGMAS) were collected from day of year (DOY) 15–19, 2019. The data have a sampling interval of 30 s. The stations both can track BDS-2 B1I and B3I, and BDS-3 B1I, B3I, and B2a signals. The stations NTSC and BRCH are located at time laboratories and connected to the high-precision atomic clock. Taking NTSC as the center node, the time link of BRCH-NTSC was designed. Details of the two stations are listed in Table 2.

Table 3 summarizes the detailed BDS PPP processing strategies. Four combined BDS (BDS2 + BDS3) PPP methods were performed. For the purpose of comparison, the BDS-2-only IF-PPP0 model, namely IF-PPP0(2) in this study, was also used. The precise BDS orbit and clock products at intervals of 15 min and 30 s, respectively, are provided by the GNSS Research Center of Wuhan University (Zhao et al. 2018; Wang et al. 2019). All the BDS satellite clocks are consistent with the IF combination of B1I and B3I. The satellite DCBs of the BDS-3 signals are provided by the Chinese Academy of Sciences (CAS) monthly product (Wang et al. 2016). The antenna file data generated by iGMAS are utilized to correct the GNSS satellite phase center offset. The dry tropospheric delay is corrected with the modified Hopfield model based on the Global Pressure and Temperature 3 (GPT3) model, and the Vienna mapping

Table 2 Details of selected stations from timing laboratories

Station	Time laboratory	Receiver	Antenna	Clock
NTSC	NTSC	CETC-54-GMR-4016	GNSS-750	H-MASER
BRCH	PTB	CETC-54-GMR-4016	NOV750.R4	H-MASER

Table 3 BDS PPP data processing strategy

| Items	Strategies
Estimator	Kalman filter
Solutions	BDS-2 IF-PPP0 [IF-PPP0(2)]; BDS B1I/B3I IF-PPP0; B1I/B3I/B2a IF-PPP1, IF-PPP2 and UC-PPP
Sampling rate	30 s
Elevation cutoff	7°
Observations weight	Elevation weight [sin(elevation)]
Satellite orbit	Fixed by Wuhan University precise orbit products
Satellite clock	Fixed by Wuhan University precise clock products
Satellite DCB	B1I: $-\beta_{1,2}^{s} \cdot DCB_{1,2}^{s}$; B3I: $\alpha_{1,2}^{s} \cdot DCB_{1,2}^{s}$; B2a: $\alpha_{1,2}^{s} \cdot DCB_{1,2}^{s} - DCB_{3,2}^{s}$
Earth rotation	Fixed (Petit and Luzum 2010)
Relativistic effect	Corrected (Kouba 2009)
Phase windup effect	Corrected (Wu et al. 1992)
Tide effect	Solid Earth, pole and ocean tide (Petit and Luzum 2010)
Satellite antenna	iGMAS values
Receiver antenna	iGMAS values
Station coordinates	Estimated as constants
Ambiguities	Estimated as constants
Tropospheric delay	Modified Hopfield for dry part and estimated for wet part (10^{-9} m²/s) (Su and Jin 2018)
Ionospheric delay	IF-PPP0/IF-PPP1/IF-PPP2: eliminated first order by IF observations; UC-PPP: estimated as white noise process (10^{4} m²/s) (Su et al. 2019b)
Receiver clock	Estimated as white noises (10^{5} m²/s)

functions 3 (VMF3) is used correspondingly to acquire the mapping functions of both dry and wet parts according to the elevation angle of each satellite (Hopfield 1969; Landskron and Böhm 2018). In the Kalman filter of the PPP processing, the station coordinate is estimated as constants. The tropospheric ZWD is estimated as a random walk process and the receiver clock is estimated as white noises. The ambiguities are estimated as constants for each epoch. The code and phase observation precision for BDS is set to 0.4 and 0.004 m, respectively. The system weighting ratio of BDS MEO/IGSO and GEO was assumed to be 10:1 (Su et al. 2019a).

Validation of the time and frequency transfer models

At this time of transition for BDS, the BDS aims to provide positioning, navigation, and timing services for global users (CSNO 2019). Figure 1 shows the distribution of PDOP values for BDS-2 and BDS (BDS-2/BDS-3) constellation on 01:00 Coordinated Universal Time (UTC)

DOY 19, 2019. The stations BRCH and NTSC are also marked in the figure. It can be seen that the BDS-2 service area is mainly centered in the Asia-Pacific region, where its GEO satellites and IGSO satellites are mainly concentrated. In conjunction with BDS-3, the BDS PDOP values are significantly reduced and the corresponding values in the Asia-Pacific region are almost less than 2. The introduction of BDS-3 widely expands the BDS global service area. Besides, the BDS-2 and BDS PDOP values of station BRCH are both larger than those at station NTSC on 01:00 UTC, DOY 19, 2019.

Figure 2 provides the visible satellites and corresponding TDOP at two stations for BDS-2 and BDS during the experimental period. The average numbers of BDS-2 visible satellites for stations NTSC and BRCH are (10.7, 10.6, 10.5, 10.7, 10.7) and (3.9, 4.1, 3.8, 3.8, 3.8) from DOY 15–19, respectively. The average TDOP values for stations NTSC and BRCH are (1.6, 1.7, 1.6, 1.6, 1.5) and (7.6, 7.2, 8.7, 5.9, 4.1) for the corresponding 5 days, respectively. The average numbers of BDS visible satellites are (14.7, 15.2, 15.0, 15.2, 15.3) and (9.4, 9.4, 9.6, 9.6, 9.6), respectively, and the average TDOP values are (1.0, 1.0, 1.0, 1.0, 1.0) and (0.9,
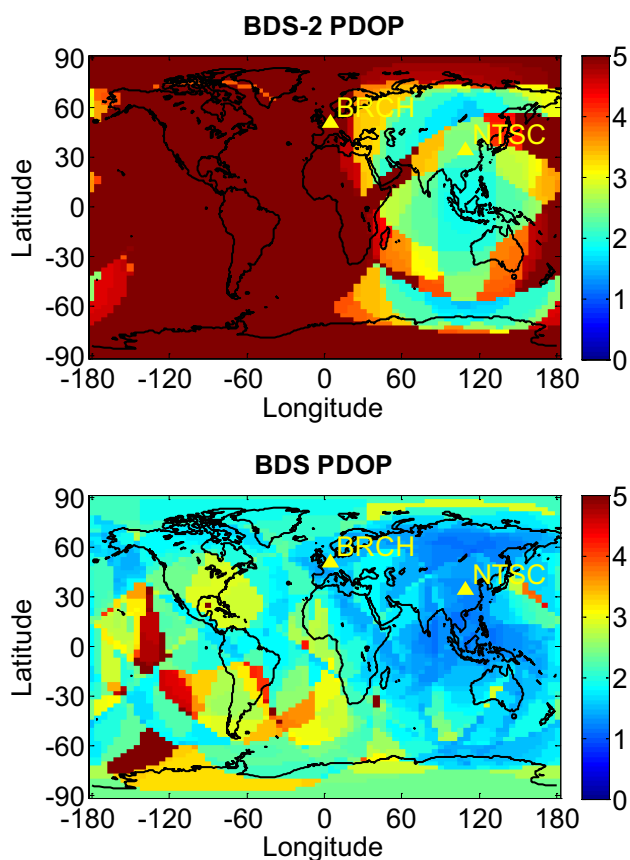
Fig. 1 Distribution of PDOP values for BDS-2 (top) and BDS (bottom) constellation on 01:00 UTC, DOY 19, 2019. Stations BRCH and NTSC are also marked

1.0, 0.9, 1.0, 0.9), respectively. The increased number of BDS-3 satellites can significantly decrease the TDOP values and improve satellite geometry. The station NTSC has more visible satellites than station BRCH, and the corresponding TDOP values are more stable.

The receiver clock offset is of great interest in the timing community. Figure 3 shows the estimated receiver clock offset for different models at two stations. The variation of the estimated receiver clock for each model is different on different days. The results also indicate that the estimated receiver clocks of the IF-PPP0, IF-PPP1, and UC-PPP models display nearly the same values, which are the combined raw receiver clock and B1I/B3I receiver hardware delays ($d\bar{t}_r = dt_r + d_{r,\mathrm{IF}_{1,2}}$). The estimable receiver clock of the IF-PPP2 model fluctuates with the same tendency but with a steady bias ($d\bar{t}_r = dt_r + d_{r,\mathrm{IF}_{1,2,3}}$). Because the two stations are connected to the high-precision atomic clock, the clock time series of the two stations for each model emerge similarly except for a system bias caused by the receiver hardware delays.

Figure 4 depicts the time difference for different PPP models on the BRCH-NTSC time link. It can be concluded
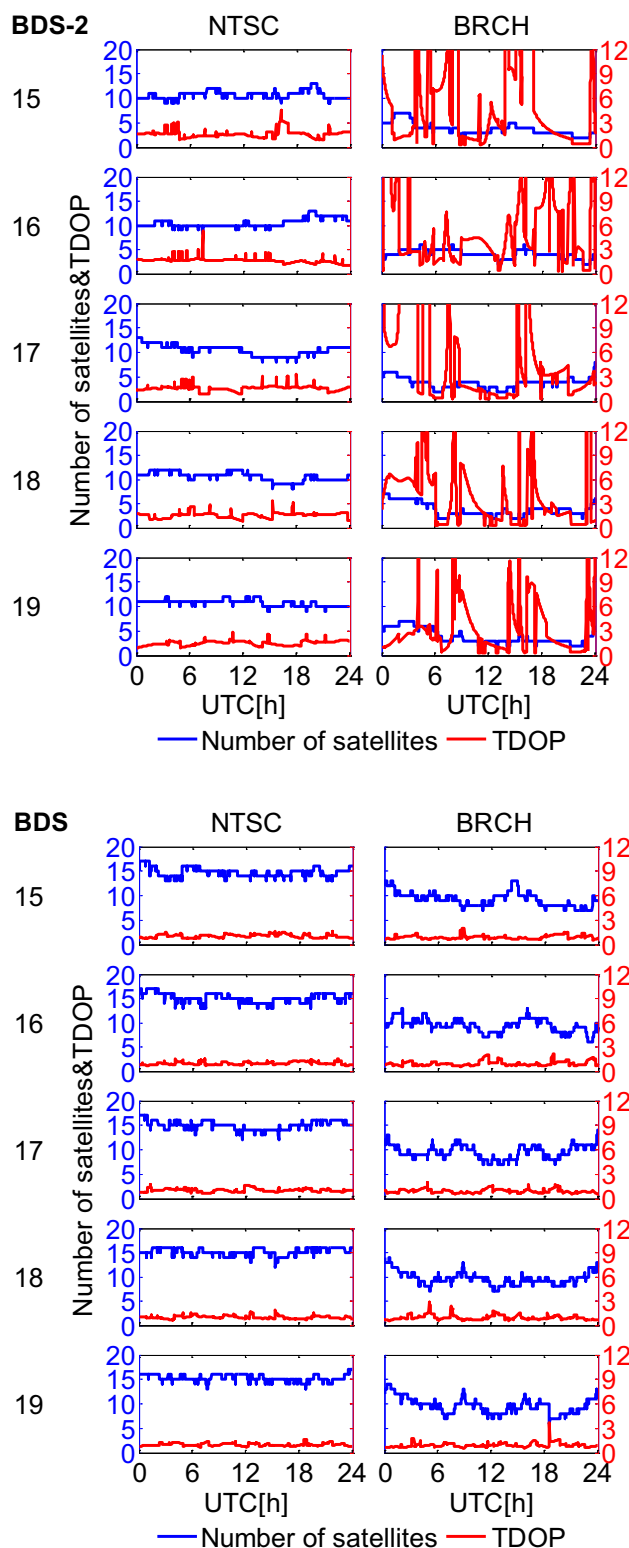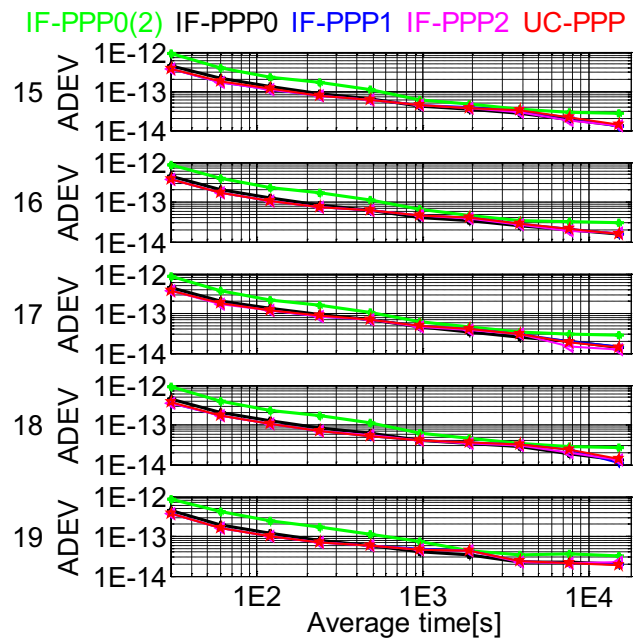

Fig. 2 Number of the visible satellites and corresponding TDOP values at stations NTSC and BRCH for BDS-2 (top) and BDS (bottom). The numbers (15–19) denote the corresponding DOY

Fig. 3 Estimated receiver clock time series of stations NTSC and BRCH for different PPP models
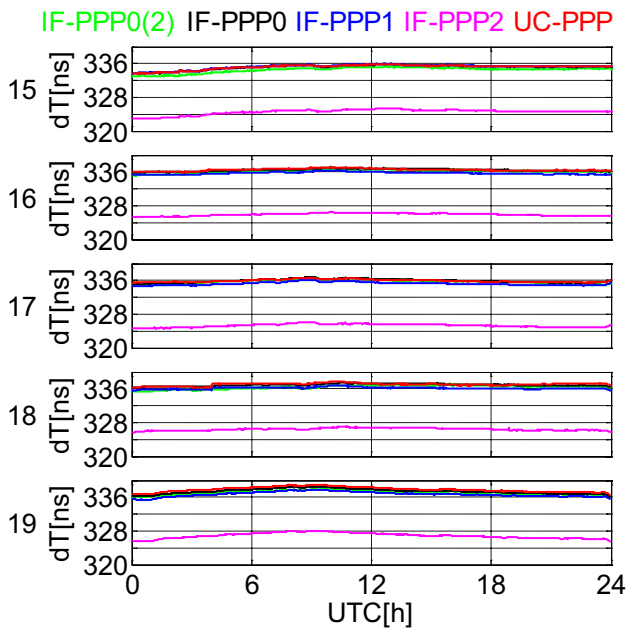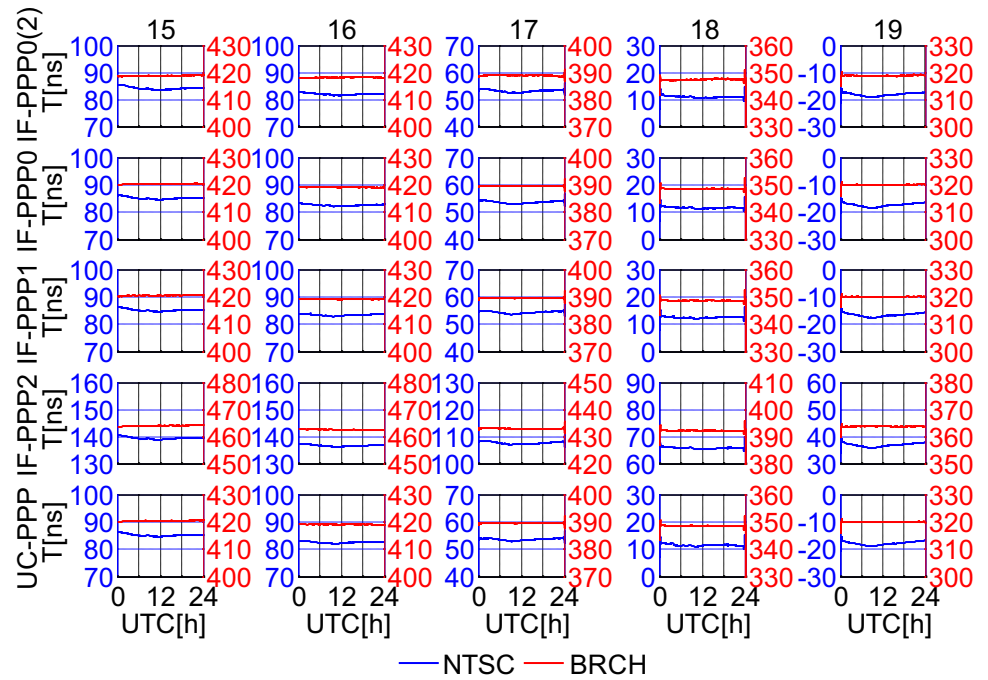
Fig. 4 Time difference for different PPP models on the time link BRCH-NTSC, where "*dT*" means "delta *T*"

Fig. 5 Allan deviation for different PPP models on the time link BRCH-NTSC

that the time difference of different PPP models is very stable on this time link over different days. As discussed before, the time difference of the two stations for the IF-PPP0, IF-PPP1, and UC-PPP is the same, which can also be clearly seen in the figure. From DOY 15 to 19, the corresponding STDs are (0.6, 0.6, 0.5, 0.5, 0.7) for IF-PPP0(2), (0.5, 0.4, 0.4, 0.3, 0.6) ns for IF-PPP0, (0.5, 0.3, 0.4, 0.2, 0.6)

ns for IF-PPP1, (0.5, 0.4, 0.4, 0.3, 0.6) ns for IF-PPP2, and (0.4, 0.3, 0.3, 0.3, 0.6) ns for UC-PPP. The time difference between the models behaved slightly different for different days. In addition, the four BDS PPP models have slightly smaller amplitudes than the BDS-2 solution.

Figure 5 illustrates the Allan deviation values of the clock difference for different PPP models on BRCH-NTSC

at different time intervals. The Allan deviation was utilized to evaluate the frequency stability of the time difference for the time link BRCH-NTSC, which was calculated by the Stable32 software (http://www.wriley.com/). It can clearly be seen that the BDS IF-PPP0 performs better than the BDS-2 solution due to the increase in the number of satellites due to BDS-3. Theoretically, the three triple-frequency CP precise and frequency transfer models are equivalent if the variance–covariance matrix is transformed according to the law of covariance propagation and the error sources are effectively corrected (Xu and Xu 2016). The slight inconsistency in the three models arises from the limited accuracy of the monthly satellite DCB products. With the upgrading of the BDS-3 daily DCB products, we can expect the BDS-3 triple-frequency CP precise time and frequency models to achieve better results. For the five continuous days, the stability of 10,000 s is better than 3×10^{-14} for the IF-PPP0(2) solution. For the dual- and triple-frequency BDS PPP models, the stability of 10,000 s is better than 1.5×10^{-14}.

In CP precise time and frequency models, the receiver coordinates were estimated as constants. Figures 6 and 7 depict the positioning error for different PPP models at stations NTSC and BRCH, respectively. The precise receiver coordinates were acquired by Bernese 5.2 software, which are precise enough to evaluate the positioning accuracy. Table 4 provides the statistic of positioning error at stations NTSC and BRCH for different solutions. The results show that the positioning errors of BDS PPP are better than those of the BDS-2 solution. The positioning errors of the three BDS triple-frequency PPP are not significantly different, and the triple-frequency PPP models perform better than the IF-PPP0 solution. The positioning performances of the PPP models at station NTSC are slightly worse than at BRCH. The receiver coordinates estimates have an accuracy of a few centimeters in CP precise time and frequency models.

In CP precise time and frequency transfer models, the tropospheric delay corrections are estimated as a random walk process. Figure 8 shows the estimated ZTD for different PPP solutions at stations NTSC and BRCH. To evaluate the accuracy of estimated ZTD, the tropospheric values derived by Bernese 5.2 software are also utilized as reference values. The RMS of ZTD error for stations NTSC and BRCH were (3.6, 2.8, 3.0, 3.1, 3.0) cm and (1.9, 1.4, 1.4, 1.4, 1.4) cm for the IF-PPP0(2), IF-PPP0, IF-PPP1, IF-PPP2 and UC-PPP solutions. For the four BDS time and frequency transfer solutions, no significant difference (maximal accuracy difference of 3 mm) was found for the accuracy of the estimated tropospheric delay.

The receiver IFB values are estimated as by-products in triple-frequency CP time and frequency transfer models. Figure 8 shows the time series of IFB estimates of IF-PPP1, IF-PPP2, and UC-PPP models at stations NTSC and BRCH. In the three models, the maximum values of receiver IFB
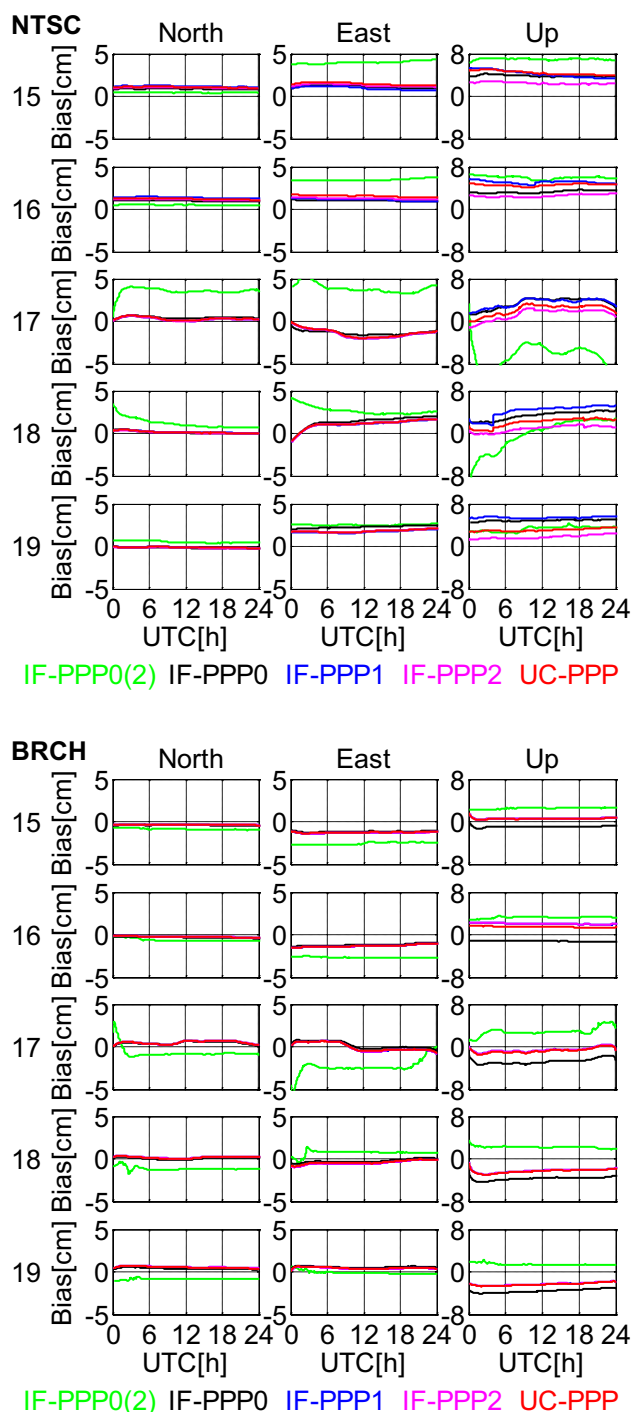

Fig. 6 Positioning error for different PPP models at stations NTSC (top) and BRCH (bottom)

estimates are approximately 5 ns, which is mainly caused by the strong correlation between the ionospheric delay and receiver DCB. According to (15) and (24), we can clearly see that the ratio of the estimated IFB in the IF-PPP1 (ifb$_{\text{IF1}}$) and UC-PPP (ifb$_{\text{UC}}$) models theoretically is $\beta_{1,3}^s$ (-1.314). To further verify the estimated IFB values of the two models,

Fig. 7 Estimated ZTD for different PPP models at stations NTSC and BRCH
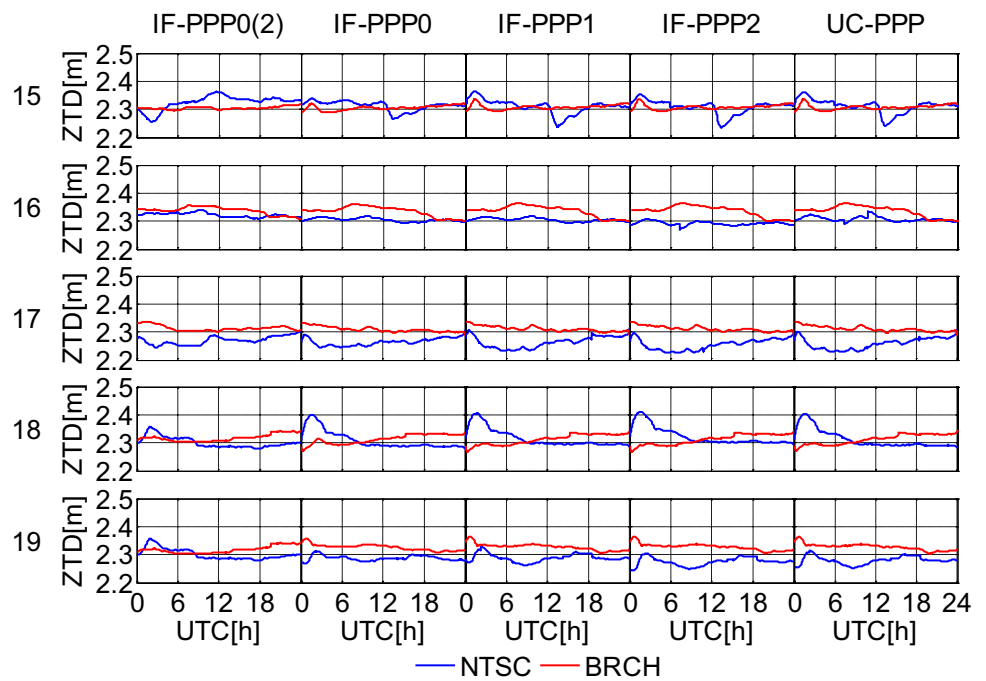
Table 4 Statistic of positioning error at NTSC and BRCH

|	RMS (mm)			STD (mm)		
	North	East	Up	North	East	Up
NTSC						
IF-PPP0(2)	19.6	39.9	68.4	13.3	31.6	36.9
IF-PPP0	5.2	34.6	45.7	4.0	27.2	34.6
IF-PPP1	6.4	37.6	50.9	5.1	31.1	37.6
IF-PPP2	5.5	34.5	27.1	4.5	28.4	34.5
UC-PPP	5.9	35.3	35.7	4.6	28.9	35.3
BRCH						
IF-PPP0(2)	9.8	13.8	20.2	3.8	12.5	13.6
IF-PPP0	3.8	7.9	29.5	3.6	6.7	12.5
IF-PPP1	4.4	7.7	16.7	3.5	6.8	11.4
IF-PPP2	4.4	7.7	16.7	3.5	6.7	11.4
UC-PPP	4.3	7.4	17.2	3.4	5.8	11.6

Fig. 9 shows the ratio of the IFB estimates ($\text{ifb}_{IF1}/\text{ifb}_{UC}$). The theoretical values $\beta^s_{1,3}$ (-1.314) are also shown in the figure. The ratio values of IFB at station BRCH fluctuate near the theoretical value. The ratio values of IFB at station NTSC fluctuate unstably, especially for DOY 18, which is mainly affected by other neglected error sources such as multipath effect. The results can further confirm our derivation of the corresponding estimable IFB parameters and their relationship.

Conclusion and discussion

This study contributed to models for CP precise time and frequency transfer with the new BDS triple-frequency signals. Three triple-frequency CP precise time and frequency transfer models, called IF-PPP1, IF-PPP2, and UC-PPP, were developed. The mathematical and stochastic models were also introduced for these models. Datasets from two stations located at time laboratories were utilized to verify the proposed models.

With the upgrading of BDS-3, the BDS has been expanded to a global service area. Comparative analysis shows that the proposed three triple-frequency PPP models

Fig. 8 Time series of IFB estimates of IF-PPP1, IF-PPP2 and UC-PPP at stations NTSC and BRCH
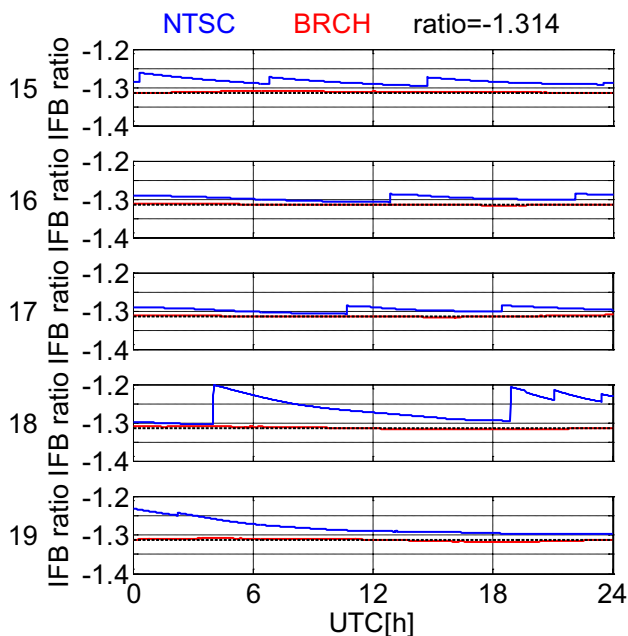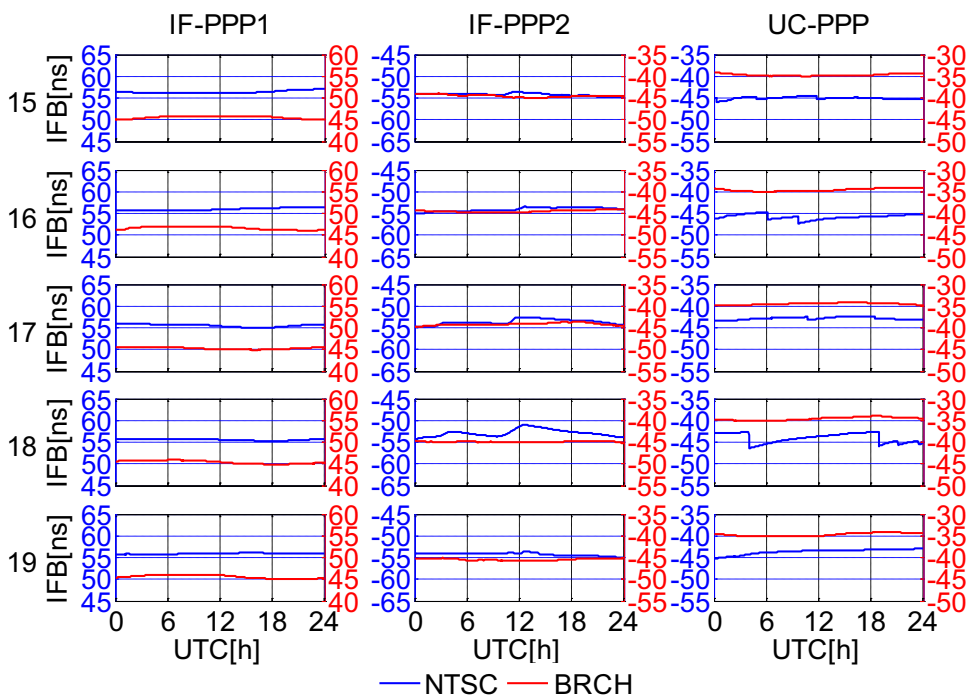
Fig. 9 Ratio of receiver IFB estimates of IF-PPP1 and UC-PPP at stations NTSC and BRCH

all can be used for precise time and frequency with the new BDS signals. With the increase in the number of BDS-3 satellites, the BDS CP precise time and frequency transfer models show better performances. The proposed models all can be applied for precise time and frequency transfer with the BDS-3 triple-frequency signals, with stability and accuracy identical to the BDS IF-PPP0 solution. The stability of 10,000 s for the proposed BDS CP precise time and frequency models is better than 1.5×10^{-14}. For these BDS time and frequency transfer models, no significant difference was found for the accuracy of the estimated positioning error and tropospheric delay. The IFB values arising from the hardware delay have to be estimated in triple-frequency PPP models. The maximum values of receiver IFB estimates are approximately 5 ns, which is mainly caused by the strong correlation between the ionospheric delay and receiver DCB.

Since the BDS-3 is still under development and undergoing upgrading, few MGEX and iGMAS stations can receive the BDS-3 multi-frequency signals. In the future, more stations for precise time and frequency with BDS-3 multi-frequency signals will be studied. The performance of BDS CP precise time and frequency transfer is expected to be further improved with more accurate orbit and clock products in the future. In addition, the UC-PPP model will lead to different results if a priori information is added on ionospheric parameters. With the upgrading of MGEX daily DCB products, more investigations should be addressed to analyze the performances of precise time and frequency transfer with the ionospheric constrained UC-PPP model.

References

CSNO (2019) BeiDou navigation satellite system signal in space interface control document—open service signal B1I (Version 3.0). China Satellite Navigation Office, Beijing

Defraigne P, Baire Q (2011) Combining GPS and GLONASS for time and frequency transfer. Adv Space Res 47(2):265–275

Defraigne P, Aerts W, Pottiaux E (2015) Monitoring of UTC (k)'s using PPP and IGS real-time products. GPS Solut 19(1):165–172

Ge Y, Qin W, Cao X, Zhou F, Wang S, Yang X (2018) Consideration of GLONASS inter-frequency code biases in precise point positioning (PPP) international time transfer. Appl Sci 8(8):1254

Hopfield HS (1969) Two-quartic tropospheric refractivity profile for correcting satellite data. J Geophys Res 74(18):4487–4499

Jiang Z, Petit G (2004) Time transfer with GPS satellites all in view. In: Proceedings Asia-Pacific workshop on time and frequency 2004, p 236

Kouba J (2009) A guide to using International GNSS Service (IGS) products. IGS Central Bureau, Jet Propulsion Laboratory, Pasadena, CA, p 34

Landskron D, Böhm J (2018) VMF3/GPT3: refined discrete and empirical troposphere mapping functions. J Geod 92(4):349–360

Larson KM, Levine L (1999) Carrier-phase time transfer. IEEE Trans Ultrason Ferroelectr Freq Control 46(4):1001–1012

Leick A, Rapoport L, Tatarnikov D (2015) GPS satellite surveying, 4th edn. Wiley, Hoboken

Montenbruck O, Hugentobler U, Dach R, Steigenberger P, Hauschild A (2011) Apparent clock variations of the block IIF-1 (SVN62) GPS satellite. GPS Solut. https://doi.org/10.1007/s10291-011-0232-x

Montenbruck O, Hauschild A, Steigenberger P, Hugentobler U, Teunissen P, Nakamura S (2013) Initial assessment of the COMPASS/BeiDou-2 regional navigation satellite system. GPS Solut 17(2):211–222. https://doi.org/10.1007/s10291-012-0272-x

Petit G, Jiang Z (2007) GPS all in view time transfer for TAI computation. Metrologia 45(1):35

Petit G, Luzum B (2010) IERS conventions (2010). No. IERS-TN-36. Bureau International des Poids et Mesures Sevres (France)

Su K, Jin S (2018) Improvement of multi-GNSS precise point positioning performances with real meteorological data. J Navig 71(6):1363–1380

Su K, Jin S, Ge Y (2019a) Rapid displacement determination with a stand-alone multi-GNSS receiver: GPS, Beidou, GLONASS, and Galileo. GPS Solut 23(2):54

Su K, Jin S, Hoque MM (2019b) Evaluation of ionospheric delay effects on multi-GNSS positioning performance. Remote Sens 11(2):171. https://doi.org/10.3390/rs11020171

Tu R, Zhang P, Zhang R, Liu J, Lu X (2018) Modeling and performance analysis of precise time transfer based on BDS triple-frequency un-combined observations. J Geod 93(6):837–847

Wang N, Yuan Y, Li Z, Montenbruck O, Tan B (2016) Determination of differential code biases with multi-GNSS observations. J Geod 90(3):209–228

Wang K, Khodabandeh A, Teunissen P (2018) Five-frequency Galileo long-baseline ambiguity resolution with multipath mitigation. GPS Solut 22:75

Wang C, Zhao Q, Guo J, Liu J, Chen G (2019) The contribution of intersatellite links to BDS-3 orbit determination: Model refinement and comparisons. Navigation 66:83–97

Wu JT, Wu SC, Hajj GA, Bertiger WI, Lichten SM (1992) Effects of antenna orientation on GPS carrier phase. Astrodynamics 18:1647–1660 (Astrodynamics 1991)

Xiao W, Liu W, Sun G (2016) Modernization milestone: BeiDou M2-S initial signal analysis. GPS Solut 20(1):125–133

Xu G, Xu Y (2016) GPS: theory, algorithms and applications, 3rd edn. Springer, Berlin

Yang Y, Li J, Xu J et al (2011) Contribution of the COMPASS satellite navigation system to global PNT users. China Sci Bull 56(26):2813–2819

Yao J, Skakun I, Jiang Z, Levine J (2015) A detailed comparison of two continuous GPS carrier-phase time transfer techniques. Metrologia 52(5):666

Zaminpardaz S, Teunissen PJ, Nadarajah N (2017) GLONASS CDMA L3 ambiguity resolution and positioning. GPS Solut 21(2):535–549

Zhang P, Tu R, Gao Y, Liu N, Zhang R (2019) Improving Galileo's carrier-phase time transfer based on prior constraint information. J Navig 72(1):121–139

Zhao Q, Wang C, Guo J, Wang B, Liu J (2018) Precise orbit and clock determination for BeiDou-3 experimental satellites with yaw attitude analysis. GPS Solut 22(1):4

Ke Su is currently a master degree candidate at the Shanghai Astronomical Observatory, Chinese Academy of Sciences, Shanghai, China. His research interests include GNSS time and frequency transfer, PPP-RTK, GNSS meteorology and GNSS seismology.
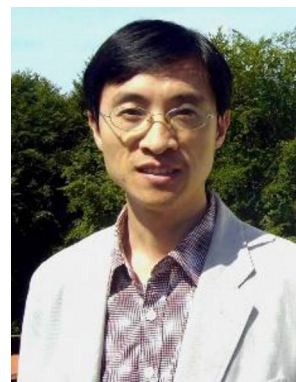
Shuanggen Jin is a Professor and Group Head at the Shanghai Astronomical Observatory, CAS. His main research areas include Satellite Navigation, Space Geodesy, Remote Sensing, Climate Change and Space/Planetary Exploration. He has received 100-Talent Program of CAS, Fellow of IAG, Fellow of IUGG, Member of Russian Academy of Natural Sciences and Member of European Academy of Sciences.